Optimum Model-Based Design of Diagnostics Experiments (DOE) with Hybrid Pulse Power Characterization (HPPC) for Lithium-Ion Batteries

Journal of The Electrochemical Society, 2024 **171** 070544

Optimum Model-Based Design of Diagnostics Experiments (DOE) with Hybrid Pulse Power Characterization (HPPC) for Lithium-Ion Batteries

Jinwook Rhyu,[1,=] Debbie Zhuang,[1,=] Martin Z. Bazant,[1,2] and Richard D. Braatz[1,z]

[1]*Department of Chemical Engineering, Massachusetts Institute of Technology, Cambridge, MA 02139, United States of America*
[2]*Department of Mathematics, Massachusetts Institute of Technology, Cambridge, MA 02139, United States of America*

Diagnostics of lithium-ion batteries are frequently performed in battery management systems for optimized operation of lithium-ion batteries or for second-life usage. However, attempting to extract dominant degradation information requires long rest times between diagnostic pulses, which compete with the need for efficient diagnostics. Here, we design a set of efficient optimal hybrid pulse power characterization (HPPC) diagnostics using model-based design of experiment (DOE) methods, applying knowledge of degradation effects on pulse kinetics and cell properties. We validate that these protocols are effective through minimization of uncertainty, and robust with Markov Chain Monte Carlo (MCMC) simulations. Contrary to traditional HPPC diagnostics which use fixed pulse magnitudes at uniformly distributed state of charges (SOC), we find that *well-designed* HPPC protocols using our framework outperform traditional protocols in terms of minimizing both parametric uncertainties and diagnostic time. Trade-offs between minimizing parametric uncertainty and total diagnostic time can be made based on different diagnostics needs.
 [DOI: 10.1149/1945-7111/ad63ce]

Manuscript submitted April 29, 2024; revised manuscript received June 30, 2024. Published July 31, 2024.

As the energy industry moves toward renewable and environmentally friendly resources such as solar and wind, energy storage is becoming increasingly important.[1] Lithium-ion batteries are ubiquitous energy storage devices that use electrochemically active particles to store and release energy through chemical reactions.[2] As lithium-ion batteries operate, degradation occurs on the active material particles while being observed at the electrode level through capacity and power loss. Battery degradation is typically assessed with macroscopic observables such as estimated reduction in capacity, which reveals little information on the internal degradation mechanisms of the active material (Fig. 1a). Determining the mechanisms behind battery failure, however, can be important to the continuous operation of a battery by the battery management system,[3] or to second-life usage and recycling procedures.[4] Direct reuse of specific electrodes is possible depending on the state of degradation of each electrode, but the design of specific second-life usage strategies is difficult unless methods are available to determine and separate the physical degradation mechanisms.[5,6]

To extract and separate degradation mechanisms dominating an electrode, many diagnostic methods have been proposed. Symptoms of degradation such as loss of lithium inventory and cathode/anode loss of active material have been extracted by recent phenomenological diagnostic methods,[7] such as area-specific impedance measurements extracted by Electrochemical Impedance Spectroscopy (EIS). However, none of these methods capture the microscopic physics behind degradation. These degradation mechanisms include formation of the solid electrolyte interphase[6] or the cathode electrolyte interphase,[8] loss of lithium in electrolyte from side reactions,[9] phase transitions and densification at the surface of nickel-rich materials,[10] particle cracking and contact loss,[11] and others. However, in many regimes, battery operation parameters (and thus degradation mechanisms) have been found to be nonidentifiable,[12–14] which indicates that mechanisms are difficult to separate from each other. Thus, *well-designed* diagnostics that can extract physical mechanisms accurately are both difficult to design and invaluable for diagnosing battery failure.

Common precise electrochemical diagnostics such as EIS are difficult to apply in battery management systems,[3] which require real-time monitoring of degradation. Data-driven methods such as (artificial) neural networks,[15,16] dynamic programming,[17] and genetic algorithms[18] have been applied to battery management systems to assess degradation and optimize operation.[19] The lack of physical modeling included in these methods, however, causes a significant loss of useful information since these systems are heavily reliant on physical mechanisms. In recent work,[20] we have shown through electrochemical simulations that pulse diagnostics can accurately extract dominant degradation mechanisms with modified Hybrid Pulse Power Characterization (HPPC) methods. However, a large amount of time is still spent performing diagnostics in these protocols.

Reducing diagnostic time while retaining accuracy is imperative for enabling online monitoring of battery health diagnostics, especially important in battery management systems for the optimized and safe operation of electric vehicles, or for efficient diagnostics to determine second-life usage of lithium-ion batteries.[21,22] Modified HPPC methods apply intermittent pulses and rests, where pulses can be powerful indicators of the power capability of a cell after degradation.[23,24] However, each pulse in a protocol requires not only a long rest time to ensure that the initial point is near equilibrium, but also a shifting time in between different values of the State of Charge (SOC). Thus, the number of accurate pulse measurements is limited. Each measurement is time-intensive, and ensuring that the necessary information is extracted and near equilibrium is crucial.

Here, we propose a framework to design the model/material-specific optimal HPPC protocol that is effective, efficient, and robust for identifying individual degradation parameters. The paper is organized as follows: The *Model description* Section describes the physical battery models applied in this study. The *Design of optimal HPPC protocols* Section describes how a set of optimal HPPC protocols are designed based on the parametric uncertainties and the total diagnostic time. The *Results and Discussion* Section provides the results and discussions of the proposed framework when applied to the Nickel-Cobalt-Aluminum (NCA)-graphite full-cell batteries. Finally, the *Conclusion* Section summarizes the overall results.

Methods

Lithium-ion batteries consist of two active material electrodes in an electrolyte bath. During (dis)charge, electrochemical energy is

[=]Equal Contribution.
[z]E-mail: braatz@mit.edu

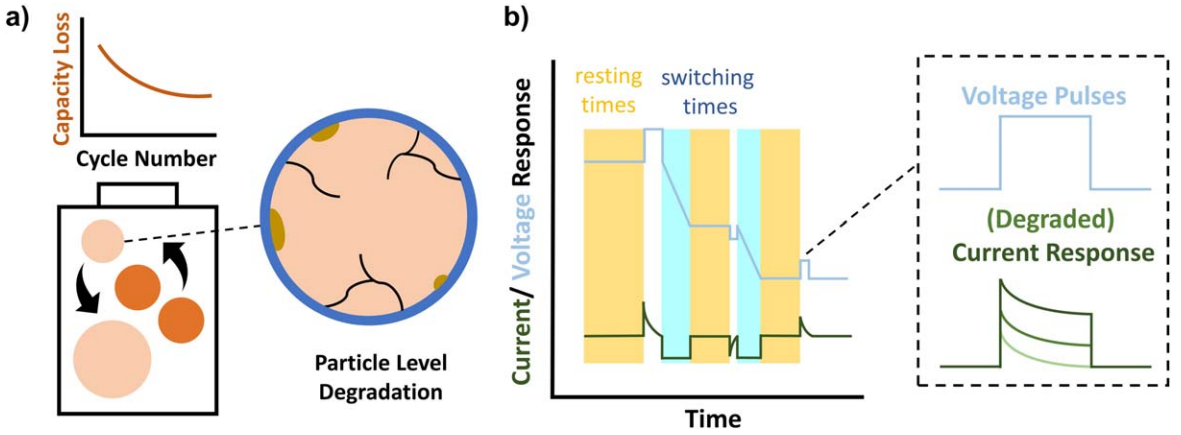

Figure 1. a) Cartoon indicating full-cell capacity loss in lithium-ion batteries due to particle-level degradation mechanisms such as film resistance growth, cracking, and surface blockage-related phase transformations. b) Diagram of an HPPC protocol, indicating the components of resting and switching times in between pulses. Rests must occur before pulses to calibrate the initial state while switching times are necessary for navigating state of charge changes. The right diagram indicates the use of current responses to voltage pulses to diagnose degradation mechanisms.

stored and released through reactions occurring at the surface of active material particles in electrodes,[25] with electrode-scale gradients supported by electrolyte transport processes. This process occurs reversibly, with intercalation switching between the cathode and the anode to transition between discharge and charge, with current or voltage control. Higher voltages release more current, providing increased power. Reaction models capture the relationship between applied current and voltage released by the electrode. Thus, accurate characterization of reaction models for current released at high voltage pulses is imperative to understanding the optimized operation of cells. As defined in Refs. 20 and 26, degradation can be characterized with the full-cell fitness W, the degraded current response relative to the nondegraded current response of a specific voltage pulse. As the current response behaves as a saturation curve after the voltage pulse (see Fig. 1b), the initial current measurement after the pulse was used for calculating W to accurately capture the kinetic information.

In Fig. 1b, in a full diagnostic protocol, the sequences usually alternate between the resting step, for equilibrating initial configurations; the pulsing step, where the current response is captured from a near-equilibrium initial state with a far-from-equilibrium perturbation for diagnostics; and the switching step, where the SOC in the cell is shifted. The expensive time requirements for each pulse from relaxation and shifting between SOCs indicate that characterizing the information content from each pulse can save expended effort in diagnostics, ultimately reducing time and energy spent on diagnostic protocols. Ultimately, enough information on the degradation state of the system needs to be extracted while minimizing the diagnostic time. In this section, we describe the simplified battery model used in this study to predict diagnostics response and our framework to design a set of optimal HPPC protocols.

Model description.—Full-cell battery models are introduced through bridging individual electrode models for the cathode and the anode. In this work, single-particle models are adopted for both electrodes as in Ref. 20. Commonly, either voltage constraints or current constraints are applied to a cell to extract electrochemical power. Cell-level voltages are constrained through the voltage drop between the cathode and the anode, $\phi_c - \phi_a$. The subscript "c" indicates cathode, while the subscript "a" indicates anode, which also holds for the later parts. Conservation between the full-cell is constrained by equating the electrode-level currents at the cathode (i_c) and the anode (i_a) to the cell-level current (i_{cell}) such that

$$f_a\, i_a(c_a, \phi_a, R_{f,a}, \tilde{c}_a, c_+) = -f_c\, i_c(c_c, \phi_c, R_{f,c}, \tilde{c}_c, c_+) = i_{cell}, \quad [1]$$

where the reaction models constraining the applied current are integral to the accurate solution of this approach. The first element inside the parenthesis of each term indicates the filling fraction of anode (c_a) and cathode (c_c), respectively. The last three elements inside the parenthesis of each term are degradation parameters where $R_{f,c}$ and $R_{f,a}$ are the film resistance of the cathode or anode, respectively, $\tilde{c}_c$ and $\tilde{c}_a$ are the surface blockage of the cathode or anode, respectively, and c_+ is the electrolyte concentration of the cell. Here, f_c and f_a relate the particle-level current to the electrode-level for the cathode and anode, respectively, which are defined as

$$f = L(1 - \varepsilon)P_L \frac{3}{\langle r_p \rangle}, \quad [2]$$

where L is the electrode length, P_L is the volume loading of the active material, ε is the porosity of the electrode material, and $\langle r_p \rangle$ is the mean particle radius assuming the particles are spherical. Electrode parameters used in our model are given in Appendix A (Table A1), while solid diffusion parameters for the timescale formulation were taken from Ref. 27.

An accurate reaction model is necessary for formulating parametric uncertainties when designing the optimal HPPC protocols. Although the standard thermodynamically reversible Butler-Volmer (BV) reaction model[25] is widely used to model electrochemical reactions, it often fails to capture limitations from electron availability in the intercalation solid. As such, the Coupled Ion-Electron Transfer (CIET) reaction model,[28,29] which was verified with X-ray visualization of intercalation materials during (dis)charge processes,[30] was used in this work to model electrochemical reactions in these materials. We can approximate this reaction using Ref. 31 with

$$i = \frac{k_0^*(\tilde{c} - c)}{\sqrt{4\pi\lambda}}(a_+ \mathcal{H}(-\eta_f, \lambda) - c\mathcal{H}(\eta_f, \lambda)), \quad [3]$$

where k_0^* is the exchange current density prefactor, c is the lithium concentration in the intercalation solid, $\tilde{c}$ is the surface blockage ratio from nickel-rich electrode surface reconstruction degradation,[26] a_+ is the activity of lithium ions in the electrolyte, and λ is the Marcus reorganization energy indicating the environmental reorganization energy in units of thermal energy ($k_B T/e$). The function $\mathcal{H}(\eta_f, \lambda)$ is defined as

$$\mathcal{H}(\eta_f, \lambda) = \frac{\sqrt{\lambda\pi}}{1 + \exp(-\eta_f)} \operatorname{erfc}\left(\frac{\lambda - \sqrt{1 + \sqrt{\lambda} + \eta_f^2}}{2\sqrt{\lambda}}\right), \quad [4]$$

where η_f is the dimensionless formal overpotential defined as $e\eta_f = e\eta - k_B T \ln(c/a_+)$ (also in units of thermal energy), given that η is the standard overpotential more common in electrochemical reactions.[32] The standard overpotential is described as

$$e\eta = (e\phi_s + \mu(c)) - (e\phi_+ + k_B T \ln a_+) + iR_f, \quad [5]$$

where $\mu(c)$ is the chemical potential of the lithium in the intercalation solid, ϕ_+ and ϕ_s are the electrical potentials of lithium ions in the electrolyte and solid, respectively, and R_f is the increased film resistance from degradation.

As derived in Ref. 20, the fitness response of the kth pulse for the full-cell, W_k, can be expressed as

$$W_k = \frac{\hat{W}_{c,k} + \hat{W}_{a,k} \frac{f_c \frac{\partial \bar{i}}{\partial \eta_{c,k}}}{f_a \frac{\partial \bar{i}}{\partial \eta_{a,k}}}}{1 + \frac{f_c \frac{\partial \bar{i}}{\partial \eta_{c,k}}}{f_a \frac{\partial \bar{i}}{\partial \eta_{a,k}}}}, \quad [6]$$

where $\hat{W}_c$ and $\hat{W}_a$ are the half-cell fitness at the cathode and the anode, respectively, which are expressed as

$$\hat{W}_{j,k} = \hat{W}_{R_f,j,k}\hat{W}_{\tilde{c},j,k}\hat{W}_{c_+,j,k} = \frac{1}{1 - R_{f,j}\frac{\partial \bar{i}}{\partial \eta}_{j,k}} \left[\frac{\tilde{c}_j - c_{j,k}}{1 - c_{j,k}}\right] \times \left[1 - \frac{\bar{i}_{red}}{\bar{i}}_{j,k} (1 - c_+) \frac{\partial \ln a_+}{\partial \ln c_+}\bigg|_{c_+=1}\right], \quad [7]$$

for $j = c, a$.[26,33] The differential conductance $\partial \bar{i}/\partial \eta$ can be derived from Eqs. 3 and 4.[a]

Design of optimal HPPC protocols.—We aim to design a set of optimal pulse settings for HPPC protocols that efficiently explore information-rich SOC range for distinguishing different degradation mechanisms. To achieve this goal, we first consider physical constraints for pulse settings. Then, we formulate the two objective functions, the parametric uncertainties using model-based Design of Experiments (DOE)[34–36], and the total diagnostic time using scaling analysis[28], which are used for constructing Pareto fronts. Lastly, we evaluate the robustness of the designed optimal HPPC protocols using Markov Chain Monte Carlo (MCMC) method.

Constraints for pulse settings.—The competition of timescales in the physical picture of a battery requires that specific physical constraints must be applied to the magnitudes of applied pulses. Different timescales from the particle-level reaction and diffusion timescales[28] to the electrode-scale transport timescales[25] compete to modify macroscopic behavior in an electrode. These constraints for the pulse settings should be defined based on heuristics in order to design practical HPPC protocols. In general, the HPPC protocol should probe the SOC values either in monotonically increasing or decreasing order to minimize the time of the total protocol (see Fig. 1). Thus, we constrain the SOC values to be monotonically increasing or decreasing in this work. The cathode filling fraction c_c was bounded from 0.4 to 0.8 to prevent extreme voltages in the nickel-rich cathodes, which cause irreversible electrochemical or mechanical damage to the electrode.[37]

Different regimes of timescale competition induce varying macroscopic behavior, such as core-shell behavior or bulk/solid quasi-equilibrium behavior[28] in single particles. The bulk/surface quasi-equilibrium behavior simplifies the understanding of degradation in a particle, which corresponds to the reaction-limitation assumptions. Thus, the main physical constraint for applying the fitness model is reaction-limitation,[26] which constrains the bounds of the voltage pulse magnitudes. Reaction-limitation is observed when the ratio between the diffusion timescale and the process timescale is small (if using parameters from the NCA-graphite electrode materials and the CIET reaction model presented in Appendix A).[28] The ratio is found to be

$$\frac{\tau_{D,c}}{\tau_{I,c}} = \frac{|i_c|\langle r_{p,c}\rangle}{3D_{min,c}F\rho_{s,c}} \sim (1 \times 10^{-5}) \times |i_{cell}|, \quad [8]$$

for the cathode and

$$\frac{\tau_{D,a}}{\tau_{I,a}} \sim (0.1) \times |i_{cell}|, \quad [9]$$

for the anode, where τ_D and τ_I are the timescales for solid diffusion and the process, respectively, i_{cell} is the cell-level applied current, D_{min} is the minimum diffusivity, F is Faraday's constant, and ρ_s is the lithium site density of active materials.

The diffusivity of the anode varies in orders of magnitude[27] and the metric is based on a rough scaling. If the upper bound for the pulse magnitude $|\Delta V|$ is set to 200 mV, the ratio of timescales approaches almost unity, indicating that the maximum voltage pulse should be in that range. Additionally, the lower bound for the pulse magnitude $|\Delta V|$ was set to 50 mV to ensure that the current response to the voltage pulse is much larger than the measurement error, which was the assumption used in Eqs. 15 and 18.

Formulation of parametric uncertainties.—In a pulse, minimizing uncertainty is helpful in determining the extent to which each degradation parameter influences the current response. From an engineering perspective, the approach for finding the optimal HPPC protocol can be formulated as model-based DOE, which searches for the optimal model input $\mathbf{u}$ that results in a model output $\mathbf{y}$ that minimizes the uncertainty of fitted model parameters $\boldsymbol{\theta}$.[34,36] In this system, $\mathbf{u}$ is a vector of pulse settings, $\boldsymbol{\theta}$ is a vector of the degradation parameters that capture cell degradation states, and $\mathbf{y}$ is a vector of the HPPC results that is used for estimating $\boldsymbol{\theta}$. The model-based DOE can be formulated as

$$\mathbf{u}^* = \arg\min_{\mathbf{u}} \Phi^{ED}(\mathbf{u}, \boldsymbol{\theta}), \quad [10]$$

where the superscript "ED" represents experiment design. The scalar information content Φ^{ED} can be one of[35]

$$\Phi^A = \mathrm{tr}(\boldsymbol{\Sigma}_{\hat{\boldsymbol{\theta}}}(\mathbf{u}, \boldsymbol{\theta})),$$
$$\Phi^D = \det(\boldsymbol{\Sigma}_{\hat{\boldsymbol{\theta}}}(\mathbf{u}, \boldsymbol{\theta})),$$
$$\Phi^E = \max_i \lambda_i(\boldsymbol{\Sigma}_{\hat{\boldsymbol{\theta}}}(\mathbf{u}, \boldsymbol{\theta})), \quad [11]$$

where $\Sigma_{\hat{\boldsymbol{\theta}}}(\mathbf{u}, \boldsymbol{\theta})$ is the covariance matrix of the estimated parameter, $\mathrm{tr}(\mathbf{A})$ is the trace of the matrix $\mathbf{A}$, $\det(\mathbf{A})$ is the determinant of $\mathbf{A}$, and $\lambda(\mathbf{A})$ are the eigenvalues of $\mathbf{A}$. We choose the D-optimality (determinant) information content, Φ^D, because of its ability to accurately integrate over the degradation ranges in parameter space.[38]

Each pulse experiment is performed at a specific SOC, defined by cathode filling fraction c_c, as well as an applied voltage ΔV to the pulse. Therefore, each pulse is characterized by $u_k = [c_{c,k}\ \Delta V_k] \in \mathbb{R}^2$. This implies that the full HPPC diagnostic protocol can be designated through $\mathbf{u} = [u_1\ u_2\ \cdots\ u_N] \in \mathbb{R}^{2N}$, where u_k is the input for the kth pulse and N is the total number

[a] $\partial\mathcal{H}/\partial\eta$ can be approximated to $\partial\mathcal{H}/\partial\eta_f$ where the derivation can be found in Eq. (D4) in Ref. 26.

of pulses. Additionally, the degradation parameters $\boldsymbol{\theta}$ are designated through

$$\boldsymbol{\theta} = [R_{\mathrm{f,c}}\ \tilde{c}_{\mathrm{c}}\ R_{\mathrm{f,a}}\ \tilde{c}_{\mathrm{a}}\ c_{+}] \in \mathbb{R}^5, \tag{12}$$

as described in the *Model description* Section. These are the main physical degradation parameters assumed in this work. Other degradation parameters can be included if their impact on reaction kinetics can be analytically expressed.

The parameters in Eq. 12 represent the main degradation mechanisms inside cells that fall into the reaction-limited regime.[28] For cells that fall into the diffusion-limited regime, other parameters related to diffusion should be considered to accurately investigate the degradation state. In this study, we assume reaction limitation and the fitness measurements are the model output, which can be expressed as $\mathbf{y} = [W_1\ W_2\ \cdots\ W_N] \in \mathbb{R}^N$.

The covariance matrix of the estimated parameters, $\Sigma_{\hat{\boldsymbol{\theta}}}(\mathbf{u}, \boldsymbol{\theta}) \in \mathbb{R}^{5\times 5}$ in Eq. 11, contains information related to the uncertainty. For parameter estimation purposes, the Cramér-Rao lower bound, which is the inverse of the Fisher Information Matrix (FIM) $\mathbf{I}(\mathbf{u}, \boldsymbol{\theta})$,[38,39] can be used to approximate the covariance matrix $\Sigma_{\hat{\boldsymbol{\theta}}}(\mathbf{u}, \boldsymbol{\theta})$.[35,36] When assuming that the output vector $\mathbf{y}$ follows the multivariate Gaussian distribution, $\mathcal{N}_N(\boldsymbol{\mu}(\boldsymbol{\theta}), \boldsymbol{\Sigma}(\boldsymbol{\theta}))$, the FIM is

$$\mathbf{I}_{mn} = \frac{\partial \boldsymbol{\mu}}{\partial \theta_m}^{\mathsf{T}} \boldsymbol{\Sigma}^{-1} \frac{\partial \boldsymbol{\mu}}{\partial \theta_n} + \frac{1}{2}\mathrm{tr}\left(\boldsymbol{\Sigma}^{-1}\frac{\partial \boldsymbol{\Sigma}}{\partial \theta_m}\boldsymbol{\Sigma}^{-1}\frac{\partial \boldsymbol{\Sigma}}{\partial \theta_n}\right), \tag{13}$$

where $\mathbf{I}_{mn}$ is mnth element of $\mathbf{I}$, $\partial\boldsymbol{\mu}/\partial\theta_m \in \mathbb{R}^{N\times 1}$ is a vector whose kth element is $\partial\mu_k/\partial\theta_m$, and $\partial\boldsymbol{\Sigma}/\partial\theta_m \in \mathbb{R}^{N\times N}$ is a matrix whose ijth element is $\partial\Sigma_{ij}/\partial\theta_m$.

When assuming sufficient rest time between each pulse, the pulses are uncorrelated. Thus, the covariance matrix of the experimental measurement as well as its inverse both become diagonal. Then, Eq. 13 is simplified as

$$\mathbf{I}_{mn} = \sum_{k=1}^{N}\left(\frac{\partial \mu_k}{\partial \theta_m}\boldsymbol{\Sigma}_{kk}^{-1}\frac{\partial \mu_k}{\partial \theta_n} + \frac{1}{2}\boldsymbol{\Sigma}_{kk}^{-2}\frac{\partial \boldsymbol{\Sigma}_{kk}}{\partial \theta_m}\frac{\partial \boldsymbol{\Sigma}_{kk}}{\partial \theta_n}\right), \tag{14}$$

where Σ_{kk} is kkth element of Σ. Each diagonal element Σ_{kk}, which corresponds to the measurement error of W_k, can be approximated by

$$|\Delta W| = \left| W - \frac{i_{\mathrm{cell}} + \Delta i}{\bar{i}_{\mathrm{cell}} + \Delta i}\right| \approx \frac{\Delta i}{\bar{i}_{\mathrm{cell}}}|1 - W|, \tag{15}$$

where Δi is the current measurement error from the cycler equipment, and i_{cell} and $\bar{i}_{\mathrm{cell}}$ are the cell-level current responses from voltage pulses with and without degradation, respectively. The last approximation in Eq. 15 holds under the assumption that the current measurement error is much less than the current responses measured. This approximation is reasonable as the measurement error is $\mathcal{O}(10^{-4})$ A·m^{-2}, whereas the current responses are $\mathcal{O}(1)$ A·m^{-2} (when the voltage pulses are $\mathcal{O}(10^2)$ mV). Thus, each diagonal element Σ_{kk} can be approximated as[b]

$$\boldsymbol{\Sigma}_{kk} = \Delta W_k^2 = \left(\frac{\Delta i}{\bar{i}_{\mathrm{cell},k}}(1 - W_k)\right)^2. \tag{16}$$

By taking a partial derivative of Eq. 16 with respect to the degradation parameter θ_m, the equation becomes

$$\frac{\partial \boldsymbol{\Sigma}_{kk}}{\partial \theta_m} = 2\sqrt{\boldsymbol{\Sigma}_{kk}}\left(-\frac{\Delta i}{\bar{i}_{\mathrm{cell},k}}\frac{\partial \mu_k}{\partial \theta_m}\right). \tag{17}$$

Combining Eqs. 14–17 with the assumption that the current measurement error is much less than the measurements themselves (identical to the assumption used in Eq. 15), the approximation for the FIM is

$$\mathbf{I} \approx \mathbf{S}^{\mathsf{T}}\boldsymbol{\Sigma}^{-1}\mathbf{S}, \tag{18}$$

where the kth row of the sensitivity matrix (i.e., the sensitivity of the kth pulse), $\mathbf{S}_k \in \mathbb{R}^{1\times 5}$, is defined as[35,36]

$$\mathbf{S}_k = \frac{\partial W_k}{\partial \boldsymbol{\theta}} = \left[\frac{\partial W_k}{\partial R_{\mathrm{f,c}}}\ \frac{\partial W_k}{\partial c_{\mathrm{c}}}\ \frac{\partial W_k}{\partial R_{\mathrm{f,a}}}\ \frac{\partial W_k}{\partial c_{\mathrm{a}}}\ \frac{\partial W_k}{\partial c_{+}}\right]. \tag{19}$$

The sensitivity matrix $\mathbf{S}$ captures the characteristics of the reaction model (e.g., CIET model or BV model) and the electrode materials (e.g., electrode size, particle size, porosity, site density, and volumetric loading of active material), which enables our framework to build model/material-specific optimal HPPC protocols. By applying Eq. 6 to Eq. 19, the kth row of the sensitivity matrix $\mathbf{S}_k$ can be expressed as

$$\mathbf{S}_k = \frac{\hat{\mathbf{S}}_{\mathrm{c},k} + \hat{\mathbf{S}}_{\mathrm{a},k}\frac{f_{\mathrm{c}}\frac{\partial \bar{i}}{\partial \eta_{\mathrm{c},k}}}{f_{\mathrm{a}}\frac{\partial \bar{i}}{\partial \eta_{\mathrm{a},k}}}}{1 + \frac{f_{\mathrm{c}}\frac{\partial \bar{i}}{\partial \eta_{\mathrm{c},k}}}{f_{\mathrm{a}}\frac{\partial \bar{i}}{\partial \eta_{\mathrm{a},k}}}}, \tag{20}$$

where the half-cell sensitivity matrices are defined as

$$\hat{\mathbf{S}}_{j,k} = \left[\frac{\partial \hat{W}_{j,k}}{\partial R_{\mathrm{f,c}}}\ \frac{\partial \hat{W}_{j,k}}{\partial \tilde{c}_{\mathrm{c}}}\ \frac{\partial \hat{W}_{j,k}}{\partial R_{\mathrm{f,a}}}\ \frac{\partial \hat{W}_{j,k}}{\partial \tilde{c}_{\mathrm{a}}}\ \frac{\partial \hat{W}_{j,k}}{\partial c_{+}}\right]. \tag{21}$$

Applying Eq. 7 to Eq. 21 results in

$$\hat{\mathbf{S}}_{\mathrm{c},k} = \left[\frac{\frac{\partial \bar{i}}{\partial \eta}_{\mathrm{c},k}\hat{W}_{\tilde{c},\mathrm{c},k}\hat{W}_{c_+,\mathrm{c},k}}{\left(1 - R_{\mathrm{f,c}}\frac{\partial \bar{i}}{\partial \eta}_{\mathrm{c},k}\right)^2}\quad \frac{\hat{W}_{R_{\mathrm{f}},\mathrm{c},k}\hat{W}_{c_+,\mathrm{c},k}}{1 - c_{\mathrm{c},k}}\quad 0\right.$$
$$\left. 0\quad \hat{W}_{R_{\mathrm{f}},\mathrm{c},k}\hat{W}_{\tilde{c},\mathrm{c},k}\frac{\bar{i}_{\mathrm{red}}}{\bar{i}}_{\mathrm{c},k}\frac{\partial \ln a_+}{\partial \ln c_+}\Big|_{c_+=1}\right], \tag{22}$$

for the sensitivity of the cathode and

$$\hat{\mathbf{S}}_{\mathrm{a},k} = \left[0\quad 0\quad \frac{\frac{\partial \bar{i}}{\partial \eta}_{\mathrm{a},k}\hat{W}_{\tilde{c},\mathrm{a},k}\hat{W}_{c_+,\mathrm{a},k}}{\left(1 - R_{\mathrm{f,a}}\frac{\partial \bar{i}}{\partial \eta}_{\mathrm{a},k}\right)^2}\quad \frac{\hat{W}_{R_{\mathrm{f}},\mathrm{a},k}\hat{W}_{c_+,\mathrm{a},k}}{1 - c_{\mathrm{a},k}}\right.$$
$$\left.\hat{W}_{R_{\mathrm{f}},\mathrm{a},k}\hat{W}_{\tilde{c},\mathrm{a},k}\frac{\bar{i}_{\mathrm{red}}}{\bar{i}}_{\mathrm{a},k}\frac{\partial \ln a_+}{\partial \ln c_+}\Big|_{c_+=1}\right], \tag{23}$$

for the sensitivity of the anode. Similarly, the derivation of $\hat{\mathbf{S}}_{\mathrm{c},k}$ and $\hat{\mathbf{S}}_{\mathrm{a},k}$ in the BV model can be found in Appendix B.

Combining Eqs. 10, 11, and 18 leads to the final DOE formulation for uncertainty minimization as

$$\Phi^{\mathrm{D}} = \det(\boldsymbol{\Sigma}_{\hat{\boldsymbol{\theta}}}(\mathbf{u}, \boldsymbol{\theta})) \approx (\det(\mathbf{S}(\mathbf{u}, \boldsymbol{\theta})^{\mathsf{T}}\boldsymbol{\Sigma}(\mathbf{u}, \boldsymbol{\theta})^{-1}\mathbf{S}(\mathbf{u}, \boldsymbol{\theta})))^{-1}, \tag{24}$$

$$\mathbf{u}^* = \arg\min_{\mathbf{u}} \Phi^{\mathrm{D}} \approx \arg\min_{\mathbf{u}} (\det(\mathbf{S}(\mathbf{u}, \boldsymbol{\theta})^{\mathsf{T}}\boldsymbol{\Sigma}(\mathbf{u}, \boldsymbol{\theta})^{-1}\mathbf{S}(\mathbf{u}, \boldsymbol{\theta})))^{-1}. \tag{25}$$

The determinant of the covariance matrix is reciprocal to the determinant of FIM $\mathbf{I}$.

[b] In this article, the subscript k implies that the variable is dependent on $u_k = [c_{\mathrm{c},k}(\text{or } c_{\mathrm{a},k})\ \Delta V_k]$.

Solving Eq. 25 requires knowledge of degradation parameters, as sensitivity $\mathbf{S}$ and the covariance matrix Σ are functions of the degradation state $\boldsymbol{\theta}$. In practice, we do not know the state of degradation before we perform the HPPC tests, which generates a "chicken-and-egg" problem. Here, we use a simple mean-field averaging approach over the feasible region Θ (that is, the range for possible degradation parameter values), which is defined as the feasible region for degradation parameters $\boldsymbol{\theta}$, to design a *generalized* HPPC protocol. The practicality of the generalized HPPC protocol will then be validated over various degradation states within the feasible region Θ in the later sections.

One DOE formulation that employs averaging is

$$\mathbf{u}^* = \arg\min_{\mathbf{u}} \langle \Phi^{\mathrm{D}} \rangle (\mathbf{u}, \boldsymbol{\Theta}), \tag{26}$$

where $\langle \Phi^{\mathrm{D}} \rangle$ is defined as the average over Θ, which can be expressed as

$$\begin{aligned} \langle \Phi^{\mathrm{D}} \rangle (\mathbf{u}, \boldsymbol{\Theta}) &= \frac{\int_{\boldsymbol{\Theta}} \Phi^{\mathrm{D}}(\mathbf{u}, \boldsymbol{\theta}) \mathrm{d}\boldsymbol{\theta}}{\int_{\boldsymbol{\Theta}} \mathrm{d}\boldsymbol{\theta}} \\ &= \frac{\int_{\boldsymbol{\Theta}} (\det(\mathbf{S}^{\mathsf{T}}(\mathbf{u}, \boldsymbol{\theta}) \boldsymbol{\Sigma}^{-1}(\mathbf{u}, \boldsymbol{\theta}) \mathbf{S}(\mathbf{u}, \boldsymbol{\theta})))^{-1} \mathrm{d}\boldsymbol{\theta}}{\int_{\boldsymbol{\Theta}} \mathrm{d}\boldsymbol{\theta}}. \end{aligned} \tag{27}$$

However, there is no explicit solution for $\langle \Phi^{\mathrm{D}} \rangle$ as Eq. 16 implies that $\bar{i}_{\mathrm{cell}}$, which cannot be solved explicitly, needs to be calculated for finding Σ. Therefore, Latin hypercube sampling,[40] widely used in various applications such as DOE,[41–43] uniformity analysis,[44–46] and uncertainty analysis[47,48] for efficiently exploring the parameter space, was used to numerically solve $\langle \Phi^{\mathrm{D}} \rangle$. Then, Eq. 27 is modified as

$$\begin{aligned} &f_{\mathrm{uncertainty}} \\ &= \log\left(\frac{1}{N_{\mathrm{Latin}}} \sum_{n=1}^{N_{\mathrm{Latin}}} (\det(\mathbf{S}^{\mathsf{T}}(\mathbf{u}, \boldsymbol{\theta}_n) \boldsymbol{\Sigma}^{-1}(\mathbf{u}, \boldsymbol{\theta}_n) \mathbf{S}(\mathbf{u}, \boldsymbol{\theta}_n)))^{-1} \right), \end{aligned} \tag{28}$$

where N_{Latin} is the number of samples used in Latin hypercube sampling from Θ and the logarithm is applied to deal with the changes in orders of magnitude. The Δi term can be removed in Σ when calculating $f_{\mathrm{uncertainty}}$ as the solution for minimizing Eq. 28 does not depend on Δi.

Formulation of diagnostic time.—The long rest times and switching times between SOCs in full diagnostic protocols are detrimental to industrial processes for batteries, such as the operation of battery management systems and second-life recycling. A practical and economic objective to minimize is the total time spent on diagnostics. The total time includes the pulse times, times spent switching between different SOCs, as well as times spent in rest states between pulses, where the latter two dominate. Minimizing total time for diagnostics while retaining information saves practical time spent on diagnostic cycles.

Relaxation times are applied before pulses to ensure a near-equilibrium initial state when a voltage pulse is applied. To formulate the relaxation times for such a system before a pulse, we use the fact that the longest timescales in battery relaxation are often from solid diffusion.[28] Thus, the most important timescale to consider is the diffusion timescale from shifts in SOC. To obtain the relaxation times for this scale, we observe the mass conservation equation in a single-particle reaction-diffusion equation,[25,49]

$$\frac{\partial c}{\partial t} = -\nabla \cdot \mathbf{j}, \tag{29}$$

with the flux $\mathbf{j}$ defined as

$$\mathbf{j} = -\frac{cD(c)}{k_{\mathrm{B}}T} \nabla \mu, \tag{30}$$

from the gradient in lithium chemical potential in the solid μ, where c is the concentration of lithium in the intercalation solid and $D(c)$ is the solid concentration-dependent diffusivity. Here, the reaction boundary condition is $-\mathbf{n} \cdot \mathbf{j} = R$, where R is the intercalation reaction rate and $\mathbf{n}$ is an orthogonal vector to the reactive surface pointing outward. A scaling relation over the volume-averaged reaction-diffusion equation indicates that the relaxation time needed to equilibrate the particle between SOC shifts based on Ref. 28 is

$$\tau_{c_{k-1} \to c_k} = \alpha_{\mathrm{time}} \frac{L^2 \Delta c}{\min\limits_{c_{k-1} < c < c_k} (cD(c))}, \tag{31}$$

where α_{time} is a scaling factor and L is a length factor which corresponds to the mean particle size $\langle r_{\mathrm{p}} \rangle$. The change in the filling fraction of the electrode, Δc, includes not only the shift between the SOCs of the previous and next pulse (c_{k-1} and c_k, respectively) but also the change of SOC due to the previous pulse such that

$$\Delta c = |c_k - c_{k-1}| + \frac{|i_{\mathrm{cell},k-1} \Delta t_{\mathrm{pulse}}|}{p \rho_{\mathrm{s}}}, \tag{32}$$

where $\Delta t_{\mathrm{pulse}}$ is the pulse time, p is an areametric capacity, ρ_{s} is the lithium site density of active material, and $i_{\mathrm{cell},k-1}$ is the cell-level applied current density during the previous pulse. As $i_{\mathrm{cell},k-1}$ is dependent on the degradation state, which is problematic as discussed in the *Formulation of parametric uncertainties* Section, it can be replaced by the nondegraded current $\bar{i}_{\mathrm{cell},k-1}$, which serves as an upper limit for the change of SOC. The second term in Eq. 32 is not considered when calculating the relaxation time before the first pulse.

Eq. 31 is the minimum necessary relaxation time based on the slowest timescale (solid diffusion) after a pulse. Thus, this necessary relaxation time in the HPPC protocol can be separated into a constant current shifting step with a specified C-rate and a relaxation step with zero applied current. There are two distinct advantages of formulating the total diagnostic time using the necessary relaxation time indicated in Eq. 31. First, Eq. 31 is a conservative metric that depends only on material properties, which ensures near-equilibrium before applying the voltage pulse. Additionally, the necessary relaxation time framework removes the dependence on the constant current step on the C-rate, simplifying the understanding of relaxation.

Therefore, the nondimensionalized total diagnostic time can be formulated by summing the necessary relaxation times indicated in Eq. 31 for each pulse, which is expressed as

$$f_{\mathrm{time}} = \sum_{k=1}^{N} \max_{j=\mathrm{c,a}} \frac{\langle r_{\mathrm{p},j} \rangle^2 \left(|c_{j,k} - c_{j,k-1}| + \frac{|\bar{i}_{\mathrm{cell},k-1} \Delta t_{\mathrm{pulse}}|}{p_j \rho_{\mathrm{s},j}} \right)}{\min\limits_{c_{j,k-1} < c_j < c_{j,k}} (c_j D_j(c_j))} \times \frac{1}{3600\ \mathrm{s}}, \tag{33}$$

where the longer relaxation time between the cathode and the anode is selected through max. Note that the scaling factor is removed from Eq. 33 as the total diagnostic time is proportional to the scaling factor, which is independent of the choice of HPPC protocol.[c]

Construction of Pareto front.—Although it is desired to minimize the parametric uncertainty extracted from the protocol, at the same time, the total time spent performing diagnostics must also be

[c]The appropriate value for α_{time} can be found based on either experimental data or physics-based simulation. The total diagnostic time will be $(f_{\mathrm{time}} \alpha_{\mathrm{time}})$ h.

controlled to reduce economic costs. Thus, optimizing the HPPC protocol can be viewed as solving the multi-objective optimization with two objective functions, $f_{\text{uncertainty}}$ and f_{time}, with physics-based constraints on pulse settings $\mathbf{u}$. The Pareto front is constructed[50,51] to visualize the trade-off between the parametric uncertainty and diagnostic time. We transform a multi-objective optimization into a single-objective problem[d] for minimizing $f_{\text{uncertainty}}$ while setting f_{time} as a time constraint, which is formulated as

$$\begin{aligned} \min_{\mathbf{u}} \quad & f_{\text{uncertainty}}(\mathbf{u}, \boldsymbol{\Theta}) \\ \text{s.t.} \quad & f_{\text{time}}(\mathbf{u}) \leqslant t_{\text{const}} \\ & \mathbf{c}_{\text{ineq}}(\mathbf{u}) \leqslant \mathbf{0}. \end{aligned} \quad [34]$$

An example of the inequality constraints $\mathbf{c}_{\text{ineq}}$ for the input vector $\mathbf{u}$ (state of charge and voltage pulse magnitudes for each pulse) is described in the *Constraints for pulse settings* Section. The constructed Pareto front guides the choice of specific diagnostics protocol under pre-defined time constraints.

In this study, Latin hypercube sampling in Eq. 28 was performed with $N_{\text{Latin}} = 1{,}000$, which is sufficient to explore a five-dimensional degradation parameter space Θ, using pyDOE3 package.[52] The maximum diagnostic time t_{const} in Eq. 34 was gradually decreased from 60 to 1.5, where the upper and lower bounds were chosen based on system-dependent heuristics. The feasible region for Θ was set to

$$\begin{aligned} 0 \leqslant \{R_{\text{f,c}}, R_{\text{f,a}}\} &\leqslant 10.0\Omega\cdot\text{m}^2, \\ 0.8 \leqslant \{\tilde{c}_{\text{c}}, \tilde{c}_{\text{a}}\} &\leqslant 1.0, \\ 0.8 \leqslant c_{+} &\leqslant 1.0, \end{aligned} \quad [35]$$

where the values were chosen based on the heuristics. Note that the film resistances have units of $\Omega \cdot \text{m}^2$ while the other degradation parameters are non-dimensionalized. Degradation parameters outside these boundaries imply that the cell is significantly degraded beyond future use.

The Python package pygmo, which is the Python implementation of pagmo,[53] with the Improved Harmony Search (IHS) algorithm[54] was used to solve the constrained optimization in Eq. 34. In order to efficiently apply the constraint that the cathode filling fractions should be a monotonic function, the input variables $c_{\text{c},k}$ can be transformed as

$$c_{\text{c},k} = 0.8 + \frac{\sum_{i=1}^{k} v_i}{\sum_{i=1}^{N+1} v_i}(0.4 - 0.8) \quad \text{for } k = 1,...,N, \quad [36]$$

where $v_1,...,v_{N+1}$ are nonnegative values between 0 and 1 while 0.8 and 0.4 are for the upper and lower bounds[e] of c_{c} as described in the *Constraints for pulse settings* Section. As a result, solving Eq. 34 finds the optimal $\mathbf{u}'^{*} = [v_1^* \cdots v_{N+1}^* \; \Delta V_1^* \cdots \Delta V_N^*] \in \mathbb{R}^{2N+1}$.

While this problem setting does not converge well even with $10{,}000N$ generations, we can effectively reduce the parameter space for v_i for faster convergence by integrating the domain knowledge into the optimization, which was shown in various studies.[55–57] For our study, we first start with solving Eq. 34 by setting $v_{N+1} = 0$ to allow the protocol to explore the full SOC range with a loose time constraint, which converges quickly. Then, we can fix v_{N+1} to a positive constant that is proportional to the tightness of the time constraint (that is, how much the diagnostic time should be further reduced). For example, the protocol can only explore up to $N/(N + v_{N+1})$ of the full SOC range for $v_{N+1} > 0$ given that $v_1,...,v_N \leqslant 1$ (see Eq. 36). Therefore, having a large v_{N+1} would lead to a shorter diagnostic time based on our physical intuition that the total diagnostic time is proportional to the SOC range the protocol explores (see Fig. 5). In this way, the convergence speed is improved by (1) decreasing the probability of guesses activating the time constraint by reducing the SOC range and (2) reducing the number of optimized parameters by one. Algorithm 1 leads to a convergence within $1{,}000N$ generations, which leads to an order of magnitude reduction in computational cost.

Algorithm 1. Modification of Eq. 34 for faster convergence

$\mathbf{u}_0'^{*} \leftarrow$ Solution for Eq. 34 with $v_{N+1} = 0$ and $t_{\text{const}} = 60$ ▷ Converges quickly.
$t_0 \leftarrow f_{\text{time}}(\mathbf{u}_0'^{*})$
if $t_{\text{const}} \geqslant t_0$ **then** ▷ Time constraint is not activated.
  $\mathbf{u}'^{*} \leftarrow \mathbf{u}_0'^{*}$
else ▷ Time constraint is activated.
  $v_{\text{ref}} \leftarrow \frac{t_0 - t_{\text{const}}}{t_0} \times \frac{N}{5}$ ▷ Tightness of t_{const}.
  $\mathbf{u}'^{*} \leftarrow$ Solution for Eq. 34 with $v_{N+1} = v_{\text{ref}}$ and the given t_{const}
end if

Evaluation of robustness via Markov Chain Monte Carlo (MCMC).—The robustness of the HPPC protocol (that is, how well the given HPPC protocol can identify various degradation states) is significant for diagnostic purposes given that there is no available degradation information before performing the test. In this work, MCMC simulations[58] are used to evaluate the robustness of the designed HPPC protocols. N_{MCMC} samples are randomly chosen from Θ and then MCMC simulations are performed to obtain the posterior distributions of each degradation parameter. The samples of $\boldsymbol{\theta}$ in this section are different from the N_{Latin} samples used for calculating $f_{\text{uncertainty}}$ to avoid overly optimistic results.

The emcee package with the parallel stretch move was used in this work, which outperforms the standard Metropolis-Hastings algorithm with a shorter correlation time and higher computational efficiency through parallelization.[59] The prior for degradation parameters was assumed to follow the uniform distribution within the feasible region Θ since there is no available information before performing the HPPC test. Initial guesses were set by uniformly distributing 24 walkers within the feasible region and we used 10,000 steps where the number of steps was chosen from the autocorrelation analysis to ensure convergence of MCMC results.[59]

Results and Discussion

This section displays the results for the Pareto front and MCMC simulations when our framework for optimizing the HPPC protocol is applied to an NCA-graphite full-cell electrode[20] with the CIET reaction model. It should be noted that the same framework can be applied to any kind of electrode combination and kinetic reaction models.

The Pareto front was constructed as shown in Fig. 2 by solving the optimization problem in Eq. 34 with the constraints $\mathbf{c}_{\text{ineq}}$ defined as in the *Constraints for pulse settings* Section. Overall, Fig. 2 clearly displays the trade-off between the parametric uncertainty ($f_{\text{uncertainty}}$) and the total diagnostic time (f_{time}). Changes in the Pareto front while increasing the number of pulses were investigated in Fig. 2a. The number of pulses was increased from five to thirteen, which are respectively the minimum number needed for identifying five degradation parameters[f] and the number of pulses where the Pareto fronts begin to cross as shown in Fig. 2a, implying convergence. It can be observed from Fig. 2a that using an increased number of pulses reduces the parametric uncertainty under the identical constraint for the total diagnostic time. Additionally, the small amount of data points at $f_{\text{time}} \geqslant 50$ (that is, the time constraint was not activated in that region) implies that $50\alpha_{\text{time}}$ h (where α_{time} can vary based on cell properties) is a sufficient diagnostic time for

[d] Constrained single-objective optimization is used to deal with the specific time constraint that will be given from the real application.

[e] The upper and lower bounds should be swapped for the monotonically increasing scenario.

[f] The minimum number of required pulses is the same as the number of degradation parameters based on Eq. 24.

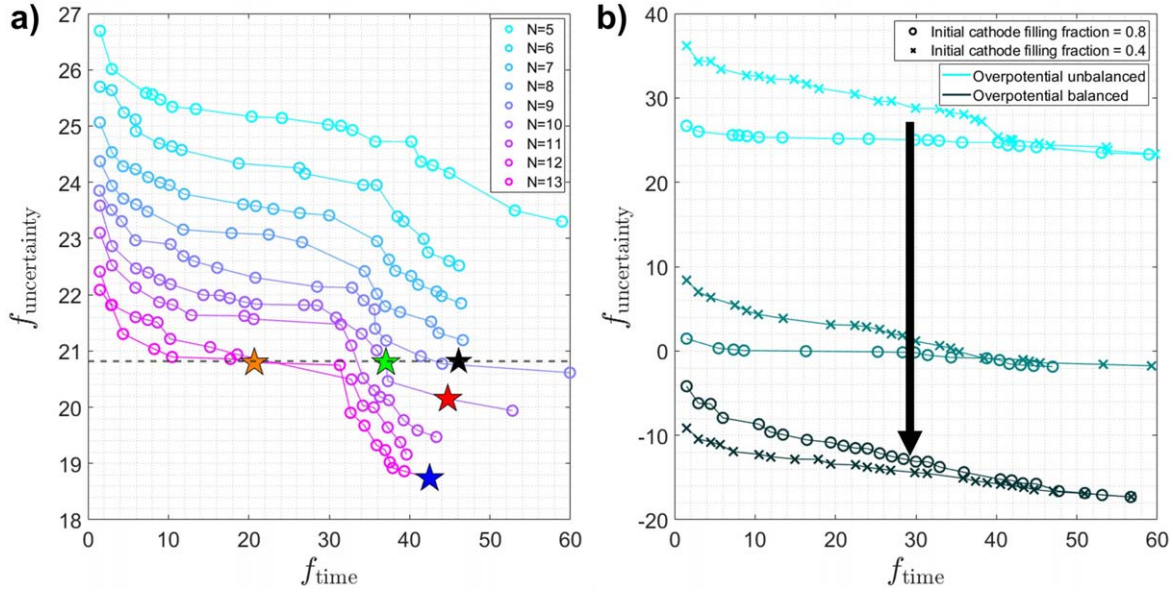

Figure 2. a) Pareto fronts for different N at a standard NCA-graphite cell. The black star indicates the standard HPPC protocol using uniformly distributed c_c values and the fixed $|\Delta V|$ value. The red and green stars are the two optimal HPPC protocols with $N = 10$, and the blue and orange stars are the optimal protocols with $N = 13$ chosen for further analysis. b) Pareto fronts for high (circle) and low (cross) initial c_c from overpotential unbalanced to balanced cells for $N = 5$. $(k^*_{0,c}, k^*_{0,a})$ values for each color are (74, 0.6), (1, 1), and (0.141, 7.08) in $A \cdot m^{-2}$ units where the last two are hypothetical scenarios.

Table I. CPU time for constructing Pareto front in units of minutes. Each Pareto front was obtained from 35 different t_{const} values varying from 60 to 1.5 with Algorithm 1. Computation was performed on 3.2 GHz 16-Core Intel i9 personal computer with 32 GB of RAM.

Fig. 2a (UB*/High**)	$N = 5$	$N = 6$	$N = 7$	$N = 8$	$N = 9$	$N = 10$	$N = 11$	$N = 12$	$N = 13$
	26	29	35	43	56	62	62	71	79
Fig. 2b ($N = 5$)	UB/High	UB/Low	MB/High	MB/Low	B/High	B/Low			
	26	26	24	27	27	28			

* UB, MB, and B stand for unbalanced, mid-balanced, and balanced scenarios, respectively, as used in Fig. 2b.
** High and Low indicate whether the initial c_c of the protocol is either 0.8 or 0.4.

extracting the maximum identifiability performance. CPU times for constructing the Pareto fronts can be found in Table I.

From the Pareto fronts constructed in Fig. 2, different optimal HPPC protocols can be selected based on the given diagnostic time constraint or the minimum requirement for accuracy. In this study, four HPPC protocols indicated as the red, green, blue, and orange stars (see Table II for descriptions) are selected for performance comparison. The specific pulse settings $\mathbf{u}$ for the chosen protocols are shown in Table III and the profiles are displayed in Fig. 3. MCMC simulations are performed on $N_{MCMC} = 100$ randomly sampled $\boldsymbol{\theta}$ from the feasible region Θ where the results are demonstrated in Fig. 4. In this study, Δi was set to 1 mA, which is the measurement error of the Maccor Series 4000. MCMC results for different Δi can be found in Appendix C (Figs. C·1 and C·2). Runtime for MCMC simulations was roughly 13.5 hours and 19 hours for $N = 10$ and $N = 13$ cases, respectively, on 3.2 GHz 16-Core Intel i9 personal computer with 32 GB of RAM.

The HPPC protocol is considered robust if it can accurately identify various combinations of degradation states $\boldsymbol{\theta}$. The performance of each HPPC protocol was evaluated using two metrics, error and uncertainty,

$$\%\ \text{error}(\theta_n) = \frac{|P_{50\%}(\theta_{n,\text{MCMC}}) - \theta_{n,\text{true}}|}{\theta_{n,\text{true}}} \times 100, \quad [37]$$

$$\%\ \text{uncertainty}(\theta_n) = \frac{P_{95\%}(\theta_{n,\text{MCMC}}) - P_{5\%}(\theta_{n,\text{MCMC}})}{\theta_{n,\text{true}}} \times 100, \quad [38]$$

where $P_{x\%}(\theta_{n,\text{MCMC}})$ indicates the xth percentile over the posterior distribution of θ_n obtained via MCMC. The main plot of each panel in Fig. 4a displays the histogram of the percentage error for 100 different degradation states $\boldsymbol{\theta}$, whereas the inset shows the histogram

Table II. Description of five HPPC protocols chosen for MCMC validation.

Name	Color	Description
Standard ($N = 10$)	Black	Traditional protocol with fixed $\|\Delta V\|$ and uniformly distributed c_c
Optimal 1 ($N = 10$)	Red	Protocol minimizing $f_{\text{uncertainty}}$ in a smaller f_{time} than standard
Optimal 2 ($N = 10$)	Green	Protocol minimizing f_{time} while maintaining $f_{\text{uncertainty}}$
Optimal 3 ($N = 13$)	Blue	Protocol minimizing $f_{\text{uncertainty}}$ in a smaller f_{time} than standard
Optimal 4 ($N = 13$)	Orange	Protocol minimizing f_{time} while maintaining $f_{\text{uncertainty}}$

Table III. Pulse settings u for the chosen HPPC protocols.

Protocol	Variable	1	2	3	4	5	6	7	8	9	10	11	12	13
Standard (Black)	c_c	.800	.800	.700	.700	.600	.600	.500	.500	.400	.400			
	ΔV (mV)	200	−200	200	−200	200	−200	200	−200	200	−200			
Optimal 1 (Red)	c_c	.800	.800	.724	.678	.676	.606	.481	.410	.410	.408			
	ΔV (mV)	−199	−199	−200	195	−200	200	−200	200	−200	200			
Optimal 2 (Green)	c_c	.800	.741	.707	.653	.645	.587	.530	.472	.418	.417			
	ΔV (mV)	−200	−200	−200	199	200	200	−200	−200	−200	200			
Optimal 3 (Blue)	c_c	.800	.800	.726	.714	.662	.655	.636	.625	.510	.405	.403	.403	.400
	ΔV (mV)	−200	−200	−200	−198	195	−200	193	192	−198	200	−200	−200	200
Optimal 4 (Orange)	c_c	.800	.800	.800	.799	.797	.734	.704	.682	.679	.664	.626	.626	.605
	ΔV (mV)	−198	200	−58	200	−199	−200	−53	−199	190	197	−196	199	−185

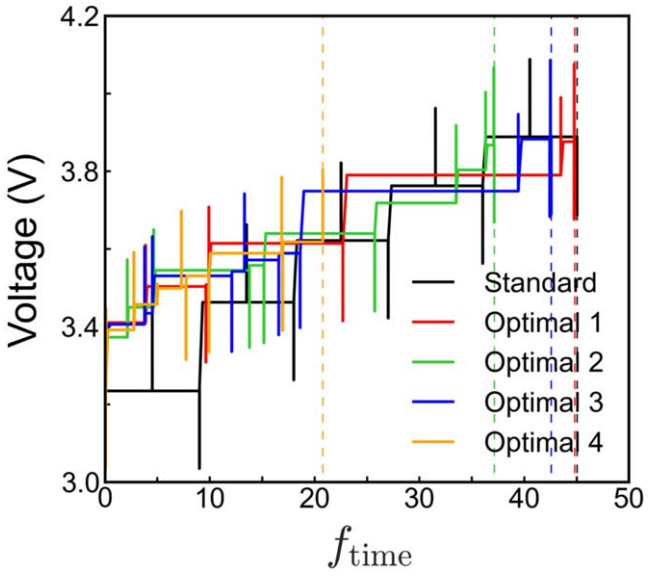

Figure 3. HPPC voltage pulse procedures plotted for standard, optimal 1, optimal 2, optimal 3, and optimal 4 protocols for comparison with respect to nondimensionalized time units rescaled by α_{time}.

of percentage uncertainty. Fig. 4b demonstrates the predicted vs. exact plots for each degradation parameter with $P_{50\%}$ in bold lines and a 90% confidence region (that is, $P_{95\%}$ and $P_{5\%}$) around them. Spikes in Fig. 4b indicate that the upper or lower bound of the confidence region deviates much from the exact value, implying that the associated degradation parameter is not well identified using the given HPPC protocol.

Comparison between the standard and optimal HPPC protocols.—The traditional approach for HPPC diagnostics uses equally spaced intervals at 10% capacity increments with equal and arbitrarily chosen rest times between the pulses.[60] Overall, the traditional approach is (1) not efficient as it does not consider the asymmetric information contained in each pulse and (2) not rigorous as it does not consider that the required rest time depends on SOC due to the order-of-magnitude changes in solid diffusivity.[27,61] In comparison, our approach starts with a sensitivity analysis comparing the information content between the pulses, assigning heavier weights to information-rich pulses. We account for the SOC dependence on relaxation time by estimating the solid diffusivity of the material to formulate the physics-based constraint on the total diagnostic time. Our approach allows an implementation of model-based optimization ($f_{\text{uncertainty}}$) with physics-based constraints (f_{time}), which gives us reliable optimal solutions.

Fig. 4a demonstrates that optimal 3 has better performance than the standard in identifying the cathode parameters by having a larger proportion with low error and uncertainty. In other words, the effectiveness of the HPPC protocol in identifying all degradation parameters improved using the proposed framework. In addition, f_{time} of optimal 4 is 20.68, which is only 45% of the standard protocol (46.09, see Figs. 2a and 3). The proposed framework can dramatically reduce the diagnostic time while retaining performance in identifiability. The trade-off between parametric uncertainties and diagnostic time is observed when comparing optimal 1/2 and 3/4, respectively, in Figs. 3 and 4a.

Overall, our framework can be used to optimize the HPPC protocol in two ways: (1) reduce the parametric uncertainties and (2) reduce the diagnostic time. While the optimal protocols chosen in this work are extreme cases where only one out of two objectives was considered, the user can balance the two objectives based on demand and the nature of physics inside the battery. For example, the MCMC results in Fig. 4 show that the improvement of optimal 3 is not large. As large improvements in identifiability are not expected, the user might focus on reducing the diagnostic time. That being said, our overall recommendation is for the optimal 4 protocol to be applied.

The position of spikes of the confidence interval varying for different HPPC protocols in Fig. 4b implies that there is no single *ultimate* HPPC protocol that shows good performance for every degradation state. In addition, the size of the confidence region for $R_{\text{f,c}}$ tends to increase as the cell degrades. This implies that identifying the degradation parameters is harder as the cell degrades. This phenomenon indicates the importance of having a *good* feasible region (that is, having a small volume around the exact degradation parameters) when designing the HPPC protocols, especially near end-of-life.

Information dependency on kinetic parameters.—The impact of the overpotential balance based on kinetic properties[20] on the Pareto front is investigated in Fig. 2b. The overpotential balance of a cell is the ratio between the required voltage drop on each electrode to extract the same full-cell current, which is highly dependent on kinetic properties as well as electrode design. Specifically, the overpotential balance is related to the differential conductance of the electrode as well as the ratio between particle-level and cell-level areas, expounded in Ref. 20. For the application in this section, the graphite electrode was found to be overpotential dominant since the NCA electrode has a higher exchange current density, which caused higher sensitivity in discharge pulses or high cathode filling fraction pulses. To understand these effects, hypothetical cells with different overpotential balances were considered by varying exchange current density prefactors at the cathode and the anode. For the overpotential unbalanced cell, the

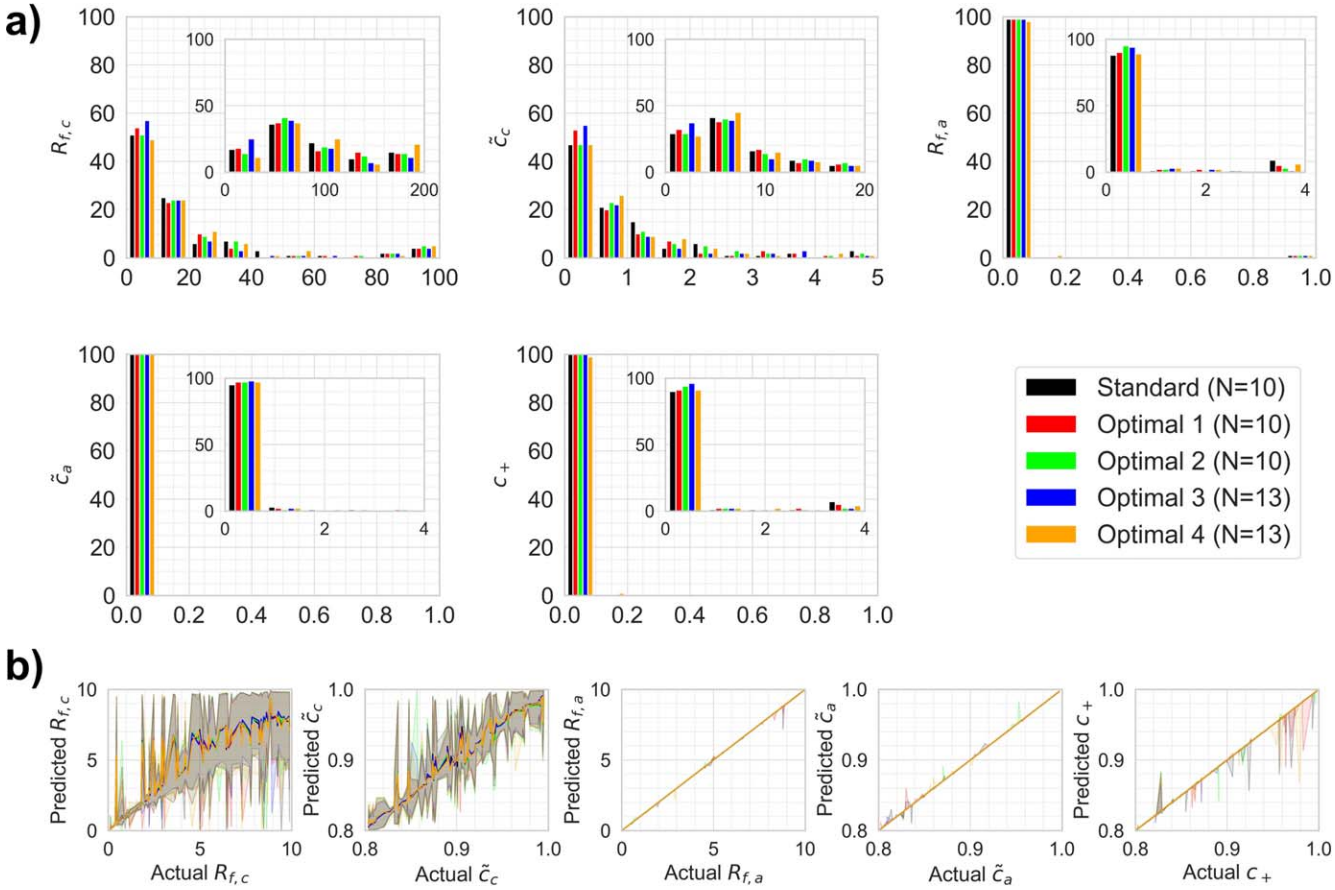

Figure 4. The performance of the standard (black) and the four optimal (red, green, blue, and orange) HPPC protocols for identifying $R_{f,c}$, $\tilde{c}_c$, $R_{f,a}$, $\tilde{c}_a$, and c_+ are evaluated via MCMC results with $\Delta i = 1$ mA. One hundred different $\boldsymbol{\theta}$ are randomly sampled from Θ to evaluate the robustness of HPPC protocols. a) The main plot of each panel displays the histogram of the percentage error whereas the inset shows the histogram of the percentage uncertainty. b) Predicted vs. exact plots for each degradation parameter with $P_{50\%}$ in bold lines and 90% confidence region marked.

standard fitted values of exchange current densities at the cathode ($k^*_{0,c} = 74$ A·m^{-2}) and the anode ($k^*_{0,a} = 0.6$ A·m^{-2}) were chosen as shown in Appendix A. Hypothetical overpotential balanced cells were used for comparison, with the final cell in Fig. 2b being a completely overpotential balanced state by setting the conductance ratio as defined in Eq. (19) in Ref. 20 to unity using scaling analysis.[g] These hypothetical cells have little variation in information extraction ability related to the initial cathode filling fraction, while the imbalanced cells vary on orders of magnitude based on the initial cathode filling fraction. It can be observed from Fig. 4 that the cathode parameters ($R_{f,c}$ and $\tilde{c}_c$) are much harder to identify than the anode parameters ($R_{f,a}$ and $\tilde{c}_a$) and electrolyte parameter (c_+). Difficulty in identifying the cathode degradation parameters was expected, as the graphite anode is the overpotential dominant electrode.[20]

Information dependency on the state of charge.—The initial configuration, or whether the diagnostic protocol is performed at a charged or discharged state, significantly influences the information extraction from pulse diagnostics as observed in Fig. 2b. For an overpotential balanced cell, the absolute information content does not depend on the initial configuration. However, for an overpotential unbalanced cell, the absolute information content from different initial configurations can be off by many orders of magnitude. Specifically, it is observed from Fig. 2b that even a short diagnostic cycle from the discharged state can have the same information content as a diagnostic cycle from the charged state with a diagnostic time twenty times longer. In contrast, this change in uncertainty is not observed for an overpotential balanced cell (note that $f_{\text{uncertainty}}$ is the logarithm of the information content). Thus, based on whether the cell is overpotential balanced or not, the initial configuration could be extremely important for designing an accurate diagnostics protocol.

To further investigate this asymmetry in information in overpotential unbalanced cells, we can track the trend of designed pulses in Fig. 3 and Table III. As the diagnostic time constraint is tightened, smaller changes in between the SOCs of the pulses are chosen. This shortens the total diagnostic time by reducing shifting and relaxation times required between pulses. When the time minimization is weighed more heavily, most pulses are designed to be at a discharged state with discharge voltage pulses (for the NCA-graphite cell with the anode being the overpotential dominant electrode). This correlates with observations in Ref. 20 where higher cathode filling fractions and discharge pulses for a similar cell have more information, decreasing parametric uncertainties. This asymmetry in information content based on SOC for an unbalanced cell explains why protocols with a short diagnostic time requirement have asymmetric information content between (dis)charged states.

To understand scaling in the trade-off of the Pareto front plot, we display the range of the cathode filling fractions explored in the protocol with respect to the diagnostic time constraint in Fig. 5. The scaling of pulse range with respect to diagnostic time is nearly linear. Additionally, the coefficients of the linear scaling between balanced or unbalanced electrodes starting at (dis)charged states are extremely similar. Practically, the range of the SOCs in a pulse protocol is related to the total relaxation time for each pulse, as defined in Eq. 33. When the cathode filling fraction changes in a pulse protocol occur in a sequential fashion, the sum of the cathode filling fraction

[g]Flip between high and low initial cathode filling fractions for the overpotential balanced cell in Fig. 2b implies that such k^*_0 values caused an overcorrection that the NCA cathode became overpotential dominant.

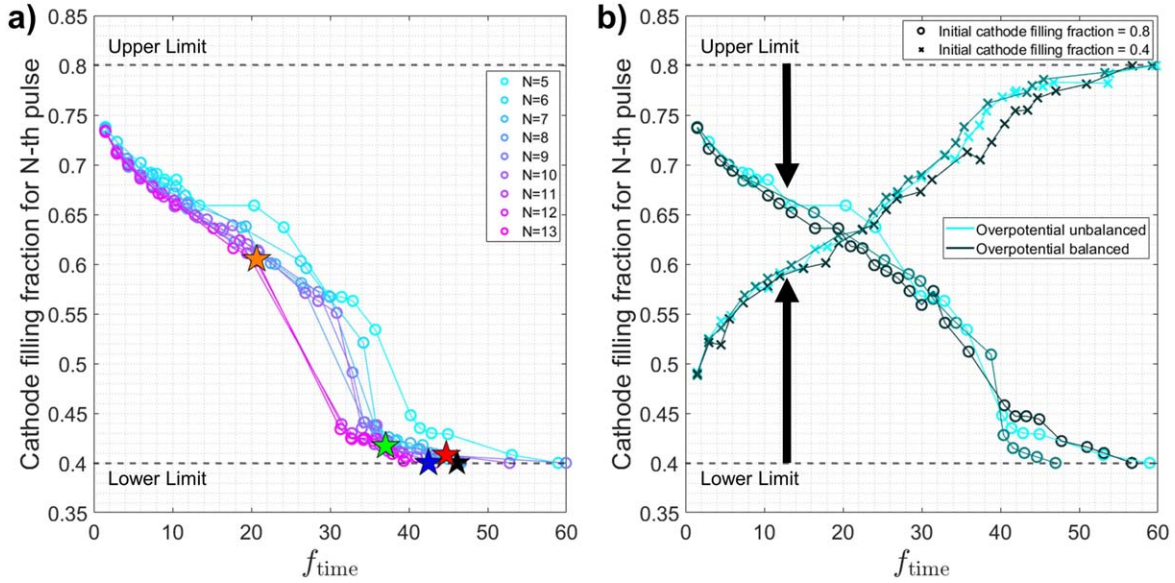

Figure 5. a) Minimum cathode filling fraction of optimally designed protocols applying different diagnostic time constraints for varying numbers of pulses $N = 5,\ldots,13$. Different optimal protocols and the standard protocol are indicated by red, green, blue, and orange stars or black stars. The initial configuration of this cell is set to be $c_{\text{c}} = 0.8$. b) Minimum or maximum cathode filling fraction of optimal protocols at different diagnostic time constraints comparing overpotential balanced or unbalanced cells. Properties of the overpotential balanced or unbalanced cells are shown in Fig. 2b. The initial configuration of this cell is either charged or discharged, indicated with different cathode filling fractions ($c_{\text{c}} = 0.4$ or 0.8).

changes in between pulses is equal to the total range of the cathode filling fraction. Frequently, either the cathode or the anode diffusivity dominates that of the entire cell, indicating that the relaxation time can be approximated as

$$f_{\text{time}} \approx \max_{j=\text{c,a}} \frac{\langle r_{\text{p},j}\rangle^2 (c_{j,\max} - c_{j,\min})}{\min_{c_{j,\min}<c<c_{j,\max}} (c_j D_j(c_j))}, \qquad [39]$$

where $c_{j,\min}$ and $c_{j,\max}$ indicate the minimum and maximum filling fraction of either cathode or anode explored during the HPPC protocol. Eq. 39 explains a nearly linear relationship between the range of the cathode filling fraction and the diagnostic time where the coefficient of this linear relationship is dependent only on material properties, specifically the solid diffusivity of the material as well as the particle size.

We emphasize the importance of this work by showing that diagnostics should not be arbitrarily designed, since pulse relaxation times should be dependent on SOC as shown in Eq. 31. Solid diffusivity changes in the material control the necessary relaxation time for each pulse. If equal relaxation times are chosen for each pulse as in arbitrarily designed HPPC, some SOCs may not have complete relaxation, while unnecessary time may be spent ensuring relaxation on others. Thus, for rigorous minimized total diagnostic time, pulses and relaxation times should be designed based on specific material properties.

Overall, we observe that the trade-off between time and accuracy occur in diagnostics due to a nearly linear relationship between the SOC range and the time constraint. However, choices of initial configurations before diagnostics can significantly influence the absolute amount of information content within the diagnostic pulses.

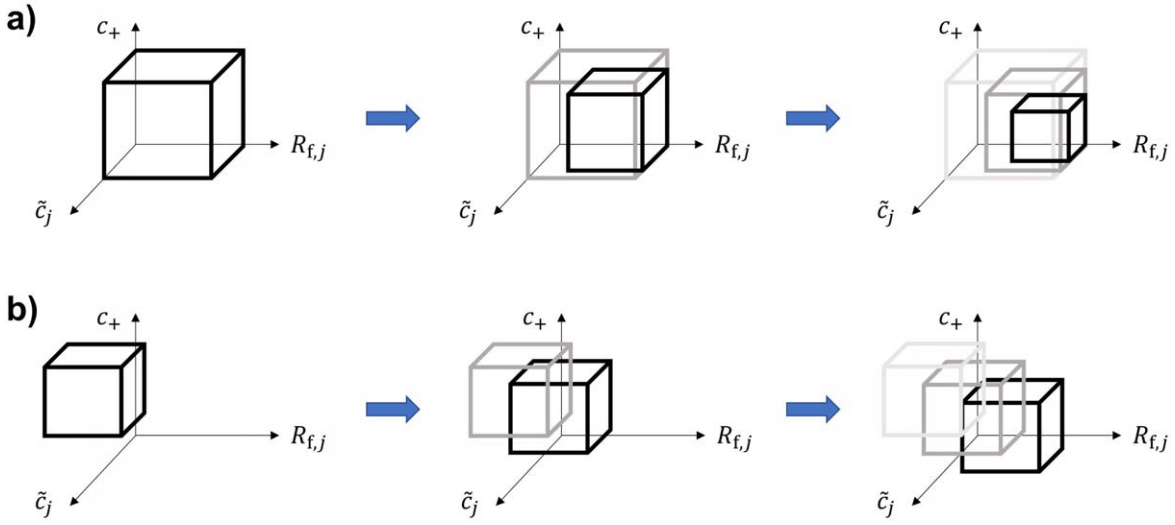

Figure 6. Graphical descriptions of the two possible approaches for incorporating the previous diagnostic results for setting the appropriate feasible region Θ. The lower bound for $R_{\text{f},j}$ and the upper bound for $\tilde{c}_j$ and c_+ are set to the estimated parameter values from the previous diagnostic results while a) the shrinking window approach uses the fixed upper bound for $R_{\text{f},j}$ and the lower bound for $\tilde{c}_j$ and c_+, and b) the sliding window approach uses the fixed length of the window. (Θ is a five-dimensional space but was reduced into a three-dimensional space in this Fig. for simplicity by introducing $j = \text{c, a}$.)

Incorporation of the previous diagnostic results.—As discussed in the *Comparison between the standard and optimal HPPC protocols* Section, it is important to set a *good* feasible region Θ that leads to a high identifiability. One main novelty of this work is how our framework adjusts the optimal HPPC protocol by incorporating previous diagnostic results. Since the degradation state of the battery cell is a monotonic function with time (that is, film resistances increase while the rescaled capacity and electrolyte concentration decrease as a function of time), the feasible region can be updated based on the previous diagnostic results. For example, a shrinking window approach (see Fig. 6a) can be considered where the least degraded corner of the feasible region Θ (the lower bound of the film resistances and the upper bound of rescaled capacity and electrolyte concentration) is updated to the degradation state $\boldsymbol{\theta}$ that was estimated from the previous diagnostic cycle, reducing the hypervolume of the feasible region Θ. Similarly, a sliding window approach (see Fig. 6b) can also be considered where the feasible region Θ is sliding toward the direction that the known degradation state $\boldsymbol{\theta}$ will move in. Analogously to the shrinking window approach, the least degraded corner of the feasible region is set to the degradation state measured from the previous diagnostics, with fixed lengths for each dimension. Overall, the boundary of the hypervolume of the feasible region can be set based on the physical heuristics of degradation bounds.

Conclusion

This study proposes a novel framework for optimizing HPPC protocols for extracting degradation information in kinetics from lithium-ion batteries by considering properties specific to the reaction model and electrode materials. A two-objective optimization was defined by formulating the parametric uncertainty for reaction-limited degradation[20] and the diagnostic time using scaling analysis.[28] Model-based DOE was used to minimize the parametric uncertainty while the diagnostic time was used as a constraint to construct the Pareto front. While the degradation state is not known a priori (which is necessary for designing the optimal HPPC protocol), a *generalized* optimal HPPC protocol was designed by applying the mean-field average approach over an expected feasible region. The robustness of the designed HPPC protocols was evaluated by performing MCMC simulations for various degradation states.

While our framework can be applied to any kind of reaction model and electrode material, the application to an NCA-graphite electrode full-cell with the CIET reaction model was demonstrated. A trade-off between the parametric uncertainty and the total diagnostic time was observed from the Pareto front (see Fig. 2). Several optimal HPPC protocols obtained from the Pareto front were compared to the standard HPPC protocol with uniformly distributed cathode filling fractions and fixed magnitude of voltage pulses. By using our framework, the total diagnostic time could be reduced relative to the standard protocol by 45% without sacrificing the identifiability performance. The information dependency on the SOC was also investigated using hypothetical overpotential balanced cells.

Although much can be learned from our optimal model-based DOE system, it must be emphasized that these methods are only applicable in reaction-limited systems for extracting degradation.[20] Exact knowledge of the relationship degradation has on the kinetics is also necessary for this model. Additionally, our system lacks experimental validation, which will be investigated in future work.

Acknowledgments

This work was supported by the Toyota Research Institute through D3BATT: Center for Data-Driven Design of Li-Ion Batteries. The authors are grateful to Yingjie Ma, Krystian Ganko, Rohan Kadambi, and Joachim Schaeffer for useful discussions. We thank Steve Pierce from SpectraPower LLC, Livermore, CA, for providing the model parameters in Appendix A.

Data and Code Availability

The data and code are available on the corresponding GitHub repository: http://github.com/JinwookRhyu/Model-based-DOE-with-HPPC-for-LiB.

CRediT Authorship Contribution Statement

Jinwook Rhyu: Conceptualization, Data curation, Formal analysis, Investigation, Methodology, Software, Validation, Visualization, Writing—original draft, Writing—review & editing. **Debbie Zhuang:** Conceptualization, Data curation, Formal analysis, Investigation, Methodology, Software, Validation, Visualization, Writing—original draft, Writing—review & editing. **Martin Z. Bazant:** Conceptualization, Formal Analysis, Funding acquisition, Project Administration, Resources, Supervision, Writing—original draft, Writing—review & editing. **Richard D. Braatz:** Conceptualization, Formal analysis, Funding acquisition, Investigation, Methodology, Project administration, Resources, Supervision, Writing—original draft, Writing—review & editing.

Appendix A. Electrode Parameter Definitions[62]

Table A1. Electrode parameters used in the *Results and Discussion* Section.

Variable Name	Definition	NCA Cathode	Graphite Anode	Units
c_0	Initial electrode concentration	0.8595	0.0142	—-
$D_{\min}$	Minimum diffusivity[27]	2.9e-15	1.54e-15	$m^2 \cdot s^{-1}$
f	Porous electrode rescaling ratio, $L(1-\varepsilon)P_L\left\langle \frac{A_p}{V_p} \right\rangle$	551	10.98	—-
k_0^*	Prefactor for exchange current density[63]	74	0.6	$A \cdot m^{-2}$
L	Length of electrode	6.4e-5	8.3e-5	m
P_L	Volumetric loading of active material	0.7452	0.8277	—-
$\langle r_p \rangle$	Mean particle radius	2e-7	1.6e-5	m
ε	Porosity	0.2298	0.1473	—-
λ	Reorganization energy of intercalation solid[63]	5	8	$k_B T$
ρ_s	Site density of electrode active materials	3.276e28	1.7438e28	m^{-3}

Appendix B. Sensitivity Analysis for Butler-Volmer Reaction

For different reaction models, the fitness values are different. For the classical BV reaction model,[25,49] the fitness at a half-cell electrode is as in Ref. 26,

$$\hat{W}_{j,k} = \left[\frac{1}{1 - R_{\mathrm{f},j}\frac{\partial \bar{i}}{\partial \eta}_{j,k}}\right]\left[\left(\frac{\tilde{c}_j - c_{j,k}}{1 - c_{j,k}}\right)^{\alpha}\right] \left[a_+^{1-\alpha}\frac{\partial a_+}{\partial c_+}\left(1 + \frac{1}{\bar{h}}\frac{\partial \ln a_+}{\partial \ln c_+}\frac{k_{\mathrm{B}}T}{e}\frac{\partial \bar{h}}{\partial \eta}(1 - c_+)\right)\right]. \quad [\mathrm{B}\cdot 1]$$

Similarly, the sensitivities for the BV model can be calculated by taking the partial derivative of $\hat{W}$ in Eq. B·1 over partial derivatives of $\boldsymbol{\theta}$. The sensitivity of the half-cell fitness for the BV model with $\alpha = 0.5$ is

$$\hat{\mathbf{S}}_{\mathrm{c},k} = \left[\frac{\frac{\partial \bar{i}}{\partial \eta}_{\mathrm{c},k}\hat{W}_{\tilde{c},\mathrm{c},k}\hat{W}_{c+,\mathrm{c},k}}{\left(1 - R_{\mathrm{f,c}}\frac{\partial \bar{i}}{\partial \eta}_{\mathrm{c},k}\right)^2} \quad \frac{\hat{W}_{R_{\mathrm{f}},\mathrm{c},k}\hat{W}_{c+,\mathrm{c},k}}{2\sqrt{(\tilde{c}_{\mathrm{c}} - c_{\mathrm{c},k})(1 - c_{\mathrm{c},k})}} \quad 0 \quad 0 \quad \frac{\hat{W}_{R_{\mathrm{f}},\mathrm{c},k}\hat{W}_{\tilde{c},\mathrm{c},k}}{2\sqrt{c_+}}\frac{\partial a_+}{\partial c_+}\left(1 + \frac{\partial \bar{h}}{\partial \eta}\bar{h}^{-1}(1 - 3c_+)\right)\right], \quad [\mathrm{B}\cdot 2]$$

for the cathode, and

$$\hat{\mathbf{S}}_{\mathrm{a},k} = \left[0 \quad 0 \quad \frac{\frac{\partial \bar{i}}{\partial \eta}_{\mathrm{a},k}\hat{W}_{\tilde{c},\mathrm{a},k}\hat{W}_{c+,\mathrm{a},k}}{\left(1 - R_{\mathrm{f,a}}\frac{\partial \bar{i}}{\partial \eta}_{\mathrm{a},k}\right)^2} \quad \frac{\hat{W}_{R_{\mathrm{f}},\mathrm{a},k}\hat{W}_{c+,\mathrm{a},k}}{2\sqrt{(\tilde{c}_{\mathrm{a}} - c_{\mathrm{a},k})(1 - c_{\mathrm{a},k})}} \quad \frac{\hat{W}_{R_{\mathrm{f}},\mathrm{c},k}\hat{W}_{\tilde{c},\mathrm{c},k}}{2\sqrt{c_+}}\frac{\partial a_+}{\partial c_+}\left(1 + \frac{\partial \bar{h}}{\partial \eta}\bar{h}^{-1}(1 - 3c_+)\right)\right], \quad [\mathrm{B}\cdot 3]$$

for the anode.

Appendix C. MCMC results for $\Delta i = 0.3$ mA and $\Delta i = 5$ mA

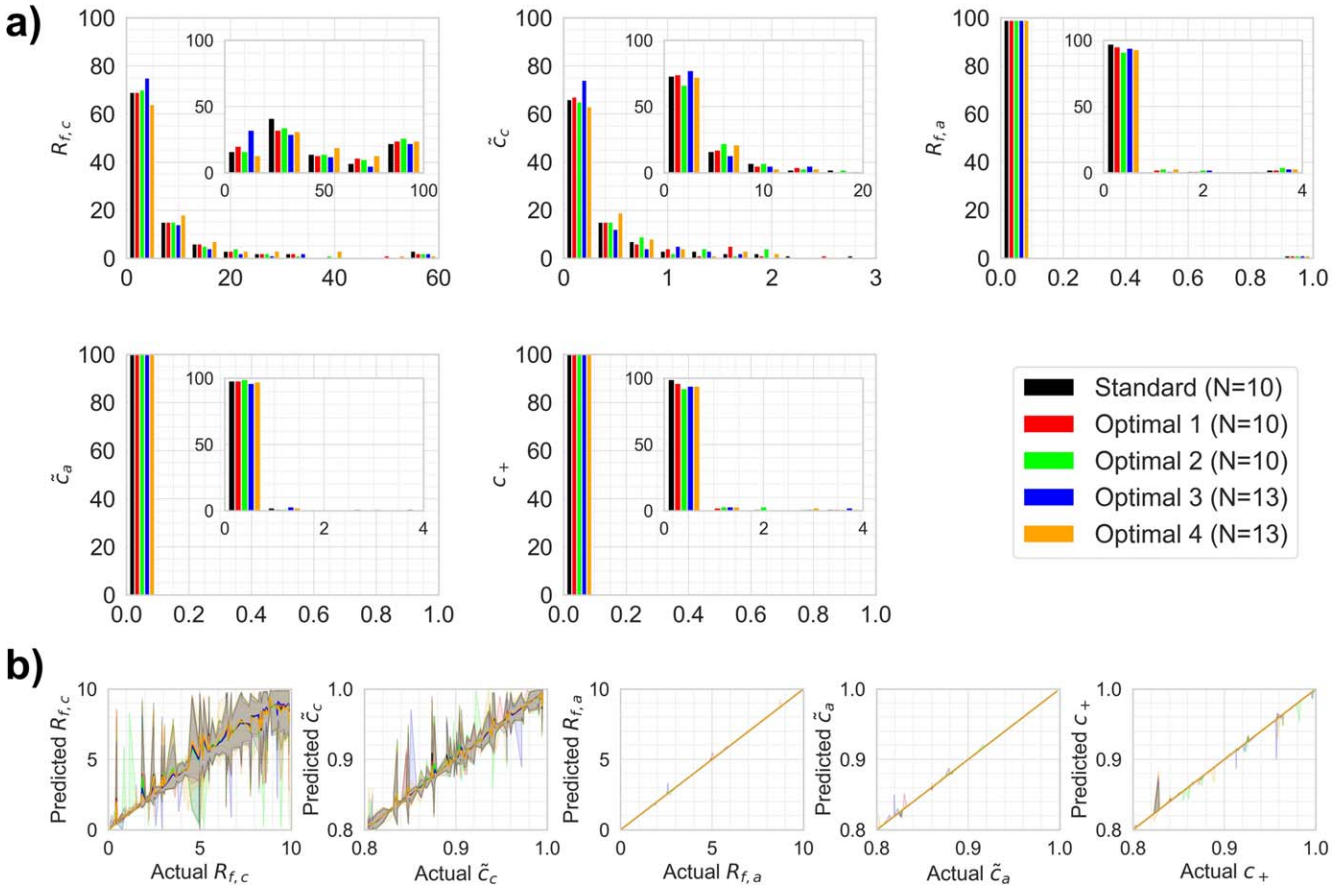

Figure C·1. The MCMC results for $\Delta i = 0.3$ mA.

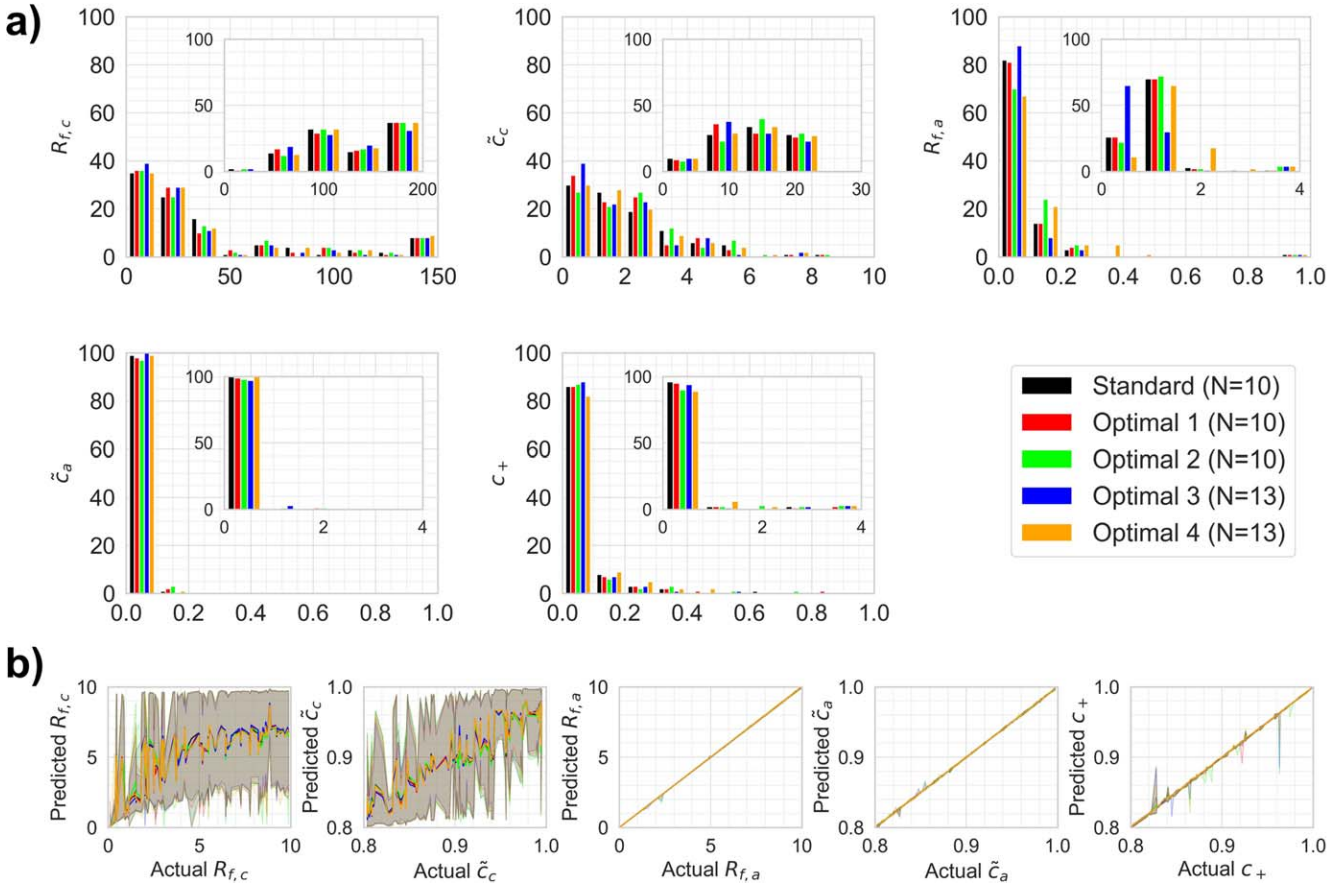

Figure C·2. The MCMC results for $\Delta i = 5$ mA.

ORCID

Jinwook Rhyu https://orcid.org/0000-0002-1198-0484
Debbie Zhuang https://orcid.org/0000-0002-1855-3768
Martin Z. Bazant https://orcid.org/0000-0002-8200-4501
Richard D. Braatz https://orcid.org/0000-0003-4304-3484

References

1. K. Kumar and B. Jaipal, *Electric Grid Modernization*, ed. M. Ghofrani (IntechOpen,, London, UK) p. 77 (2022), Chap. 5.
2. M. Li, J. Lu, Z. Chen, and K. Amine, *Adv. Mater.*, **30**, 1800561 (2018).
3. J. Zhang and J. Lee, *J. Power Sources*, **196**, 6007 (2011).
4. Y. Tao, C. D. Rahn, L. A. Archer, and F. You, *Sci. Adv.*, **7**, eabi7633 (2021).
5. D. Zhuang and M. Z. Bazant, *J. Electrochem. Soc.*, **169**, 100536 (2022).
6. M. B. Pinson and M. Z. Bazant, *J. Electrochem. Soc.*, **160**, A243 (2012).
7. C. R. Birkl, M. R. Roberts, E. McTurk, P. G. Bruce, and D. A. Howey, *J. Power Sources*, **341**, 373 (2017).
8. Q. Li, Y. Wang, X. Wang, X. Sun, J.-N. Zhang, X. Yu, and H. Li, *Journal ACS Appl. Mater. Interfaces*, **12**, 2319 (2019).
9. X. Han, L. Lu, Y. Zheng, X. Feng, Z. Li, J. Li, and M. Ouyang, *eTransportation*, **1**, 100005 (2019).
10. D. Mohanty et al., *Sci. Rep.*, **6**, 26532 (2016).
11. R. Ruess, S. Schweidler, H. Hemmelmann, G. Conforto, A. Bielefeld, D. A. Weber, J. Sann, M. T. Elm, and J. Janek, *J. Electrochem. Soc.*, **167**, 100532 (2020).
12. M. D. Berliner, H. Zhao, S. Das, M. Forsuelo, B. Jiang, W. H. Chueh, M. Z. Bazant, and R. D. Braatz, *J. Electrochem. Soc.*, **168**, 090546 (2021).
13. G. Galuppini, M. D. Berliner, H. Lian, D. Zhuang, M. Z. Bazant, and R. D. Braatz, *J. Power Sources*, **580**, 233272 (2023).
14. G. Galuppini, M. D. Berliner, D. A. Cogswell, D. Zhuang, M. Z. Bazant, and R. D. Braatz, *J. Power Sources*, **573**, 233009 (2023).
15. G. May and A. El-Shahat, "Battery-degradation model based on the ANN regression function for EV applications." *IEEE Global Humanitarian Technology Conference*, San Jose, CA p. 1–3 (2017).
16. N. Guo, X. Zhang, Y. Zou, L. Guo, and G. Du, *Energy*, **214**, 119070 (2021).
17. Y. Wang, S. J. Moura, S. G. Advani, and A. K. Prasad, *Int. J. Hydrogen Energy*, **44**, 8479 (2019).
18. P. Qiang, P. Wu, T. Pan, and H. Zang, *Energies*, **14**, 7919 (2021).
19. M. Fanoro, M. Božanić, and S. Sinha, *Energies*, **15**, 5889 (2022).
20. D. Zhuang, M. L. Li, V. N. Lam, R. D. Braatz, W. Chueh, and M. Z. Bazant, *J. Electrochem. Soc.*, **171**, 050510 (2024).
21. J. Zhu et al., *Cell Rep. Phys. Sci.*, **2**, 100537 (2021).
22. M. Shahjalal, P. K. Roy, T. Shams, A. Fly, J. I. Chowdhury, M. R. Ahmed, and K. Liu, *Energy*, **241**, 122881 (2022).
23. A. G. Li, A. C. West, and M. Preindl, *J. Power Sources*, **580**, 233328 (2023).
24. A. G. Li, W. Wang, A. C. West, and M. Preindl, *Appl. Energy*, **315**, 119005 (2022).
25. J. Newman and N. P. Balsara, *Electrochemical Systems* (John Wiley & Sons, New York, NY) 4th ed. (2021).
26. D. Zhuang and M. Z. Bazant, *Phys. Rev. E*, **107**, 044603 (2023).
27. S. Carelli, M. Quarti, M. C. Yagci, and W. G. Bessler, *J. Electrochem. Soc.*, **166**, A2990 (2019).
28. D. Fraggedakis, N. Nadkarni, T. Gao, T. Zhou, Y. Zhang, Y. Han, R. M. Stephens, Y. Shao-Horn, and M. Z. Bazant, *Energy Environ. Sci.*, **13**, 2142 (2020).
29. M. Z. Bazant, *Faraday Discuss.*, **246**, 60 (2023).
30. H. Zhao et al., *Nature*, **621**, 289 (2023).
31. Y. Zeng, R. B. Smith, P. Bai, and M. Z. Bazant, *J. Electroanal. Chem.*, **735**, 77 (2014).
32. A. J. Bard, L. R. Faulkner, and H. S. White, *Electrochemical Methods: Fundamentals and Applications* (John Wiley & Sons, New York, NY) 3rd ed. (2022).
33. D. Fraggedakis, M. McEldrew, R. B. Smith, Y. Krishnan, Y. Zhang, P. Bai, W. C. Chueh, Y. Shao-Horn, and M. Z. Bazant, *Electrochim. Acta*, **367**, 137432 (2021).
34. J. V. Beck and K. J. Arnold, *Parameter Estimation in Engineering and Science* (John Wiley & Sons,, New York, NY) 4th ed. (1977).
35. G. Franceschini and S. Macchietto, *Chem. Eng. Sci.*, **63**, 4846 (2008).
36. T. Barz, D. C. López Cárdenas, H. Arellano-Garcia, and G. Wozny, *AIChE J.*, **59**, 1981 (2013).
37. T. Li, X.-Z. Yuan, L. Zhang, D. Song, K. Shi, and C. Bock, *Electrochem. Energy Rev.*, **3**, 43 (2020).
38. K. J. Beers, *Numerical Methods for Chemical Engineering: Applications in MATLAB* (Cambridge University Press, Cambridge, UK) 1st ed. (2007).
39. P. Pakrooh, A. Pezeshki, L. L. Scharf, D. Cochran, and S. D. Howard, *IEEE Trans. Signal Process.*, **63**, 6423 (2015).
40. M. Stein, *Technometrics*, **29**, 143 (1987).
41. E. R. van Dam, B. Husslage, D. den Hertog, and H. Melissen, *Oper. Res.*, **55**, 158 (2007).
42. F. A. Viana, G. Venter, and V. Balabanov, *Int. J. Numer. Meth. Eng.*, **82**, 135 (2010).
43. F. A. Viana, *Qual. Reliab. Eng. Int.*, **32**, 1975 (2016).
44. J. L. Deutsch and C. V. Deutsch, *J. Stat. Plan. Inference*, **142**, 763 (2012).

45. M. Yourdkhani and P. Hubert, *ACS Appl. Mater. Interfaces*, **5**, 35 (2013).
46. J. Rhyu, D. Kim, and J. Nam, *Measurement*, **168**, 108420 (2021).
47. M. D. McKay, "Latin hypercube sampling as a tool in uncertainty analysis of computer models." *Winter Simulation Conference*, Arlington, VA 557 (1992).
48. J. C. Helton and F. J. Davis, *Reliab. Eng. Syst. Saf.*, **81**, 23 (2003).
49. M. Z. Bazant, *Acc. Chem. Res.*, **46**, 1144 (2013).
50. M. Ehrgott, *Multicriteria Optimization* (Springer Science & Business Media, Berlin, Germany) 2nd ed. vol 491 (2005).
51. N. Gunantara, *Cogent Eng.*, **5**, 1502242 (2018).
52. R. Lafage et al., "relf/pyDOE3: 1.0.2." (2024).
53. F. Biscani and D. Izzo, *J. Open Source Softw.*, **5**, 2338 (2020).
54. M. Mahdavi, M. Fesanghary, and E. Damangir, *Appl. Math. Comput.*, **188**, 1567 (2007).
55. W. Bi, G. C. Dandy, and H. R. Maier, *Environ. Model. Softw.*, **69**, 370 (2015).
56. W. Bi, G. C. Dandy, and H. R. Maier, *J. Water Resour. Plan. Manag.*, **142**, 04016027 (2016).
57. Z.-k. Feng, W.-j. Niu, C.-t. Cheng, and X.-y. Wu, *J. Clean. Prod.*, **171**, 390 (2018).
58. S. Brooks, A. Gelman, G. L. Jones, and X.-L. Meng, *Handbook of Markov Chain Monte Carlo* (Chapman & Hall/CRC, Boca Raton, FL) 1st ed. (2011).
59. D. Foreman-Mackey, D. W. Hogg, D. Lang, and J. Goodman, *Publ. Astron. Soc. Pac.*, **125**, 306 (2013).
60. D. H. Doughty and C. C. Crafts, *FreedomCAR: electrical energy storage system abuse test manual for electric and hybrid electric vehicle applications* (2006).
61. R. Amin, D. B. Ravnsbæk, and Y.-M. Chiang, *J. Electrochem. Soc.*, **162**, A1163 (2015).
62. M. D. Berliner, "Simulating, Controlling, and Understanding Lithium-ion Battery Models." *Ph.D. thesis*, Massachusetts Institute of Technology (2023).
63. Y. Zhang et al., *ChemRxiv*, **N/A**, N/A (2024).